

Xiangmeng Meng, Marcel Bachmann, Antoni Artinov, Michael Rethmeier

A study of the magnetohydrodynamic effect on keyhole dynamics and defect mitigation in laser beam welding

Open Access via institutional repository of Technische Universität Berlin

Document type

Journal article | Accepted version

(i. e. final author-created version that incorporates referee comments and is the version accepted for publication; also known as: Author's Accepted Manuscript (AAM), Final Draft, Postprint)

This version is available at

<https://doi.org/10.14279/depositonce-16458>

Citation details

Meng, X., Bachmann, M., Artinov, A., & Rethmeier, M. (2022). A study of the magnetohydrodynamic effect on keyhole dynamics and defect mitigation in laser beam welding. In *Journal of Materials Processing Technology* (Vol. 307, p. 117636). Elsevier BV. <https://doi.org/10.1016/j.jmatprotec.2022.117636>.

Terms of use

This work is protected by copyright and/or related rights. You are free to use this work in any way permitted by the copyright and related rights legislation that applies to your usage. For other uses, you must obtain permission from the rights-holder(s).

A study of the magnetohydrodynamic effect on keyhole dynamics and defect mitigation in laser beam welding

Xiangmeng Meng^{a,*}, Marcel Bachmann^a, Antoni Artinov^a, Michael Rethmeier^{b,a,c}

^a BAM Federal Institute for Materials Research and Testing, Unter den Eichen 87, 12205 Berlin, Germany

^b Technische Universität Berlin, Institute of Machine Tools and Factory Management, Pascalstraße 8-9, 10587 Berlin, Germany

^c Fraunhofer IPK, Pascalstraße 8-9, 10587 Berlin, Germany

Corresponding author: xiangmeng.meng@bam.de

Abstract

In this paper, the highly transient keyhole dynamics, e.g., laser absorption, keyhole geometry, and fluctuation, etc., under a magnetic field are investigated using an experimental approach and multi-physical modeling. The model provides accurate predictions to the variation of penetration depth and weld pool profiles caused by the MHD effect, which is validated by the measurements of optical micrographs and *in-situ* metal/glass observation. The micro-X-ray computed tomography shows a remarkable reduction of keyhole-induced porosity with the magnetic field. The correlation between the porosity mitigation and the weld pool dynamics influenced by the magnetic field is built comprehensively. It is found that the magnetic field gives a direct impact on the laser energy absorption at the keyhole front wall by changing the protrusion movement. The porosity mitigation comes from multiple physical aspects, including keyhole stabilization, widening of the bubble floating channel, and the electromagnetic expulsive force. Their contributions vary according to the bubble size. The findings provide a deeper insight into the relationship between electromagnetic parameters, keyhole dynamics, and suppression of keyhole-relevant defects.

Keywords: laser beam welding (LBW), keyhole dynamics, porosity, magnetohydrodynamics (MHD), X-ray computed tomography, multi-physical modeling

1. Introduction

Nowadays, more industrial applications of high-power deep penetration laser beam welding (LBW) have been realized due to the rapid development and easier access to laser sources. The LBW has several well-known superiorities compared with the conventional arc welding techniques, including highly localized but relatively lower energy input, superior penetration capacity, higher welding speed, narrower heat-affected zone, etc. In comparison to electron beam welding, the LBW does not require extra vacuum equipment for beam propagation. In addition, it is applicable to join

all industry-relevant metals including steels, Al alloys, Ti alloys, etc. Yet, not only the typical autogenous LBW but also its modifications, e.g., wire feed laser beam welding or laser-arc hybrid welding, confront several limitations in their practical applications due to defect formation such as spatter, hot-cracking, porosity, as well as inhomogeneous element distribution if filler material is applied. It has been well recognized that these issues are all closely correlated with the unique keyhole dynamics, weld pool geometry and the complex melt flow therein.

Since the last two decades, the magnetohydrodynamic (MHD) technique has also drawn more attention to enhancing the LBW process, in which a proper magnetic field is applied to control the liquid metal flow. With an external magnetic field, an eddy current can be induced in the electrically conducting fluid, namely liquid metal in this study. A volumetric Lorentz force will be generated by the eddy current and the magnetic field itself, whose force density can be described as follows:

$$\vec{F}_L = \vec{j} \times \vec{B} = \sigma_e (\vec{v} \times \vec{B} + \vec{E}) \times \vec{B} \quad (1)$$

By choosing proper frequency, magnetic flux density, and orientation of the magnetic field, desirable effects such as acceleration, deceleration, supporting, or stirring can be produced purposefully.

The beneficial effect of an external magnetic field on the LBW process was firstly reported by Kern *et al* (2000)., in which the weld pool was stabilized to eliminate the humping defects forming at high welding speed. The studies of Xu *et al.* (2020) suggested that a transverse oscillating magnetic field applied at the bottom of the workpiece was able to provide effective support against the gravity during full penetration LBW. Similar results were also achieved with a steady magnetic field of 200 mT during the full penetration LBW of Al alloy by Chen *et al.* (2017). Furthermore, it has been confirmed experimentally that the electromagnetic stirring (EMS) induced by an external magnetic field can enhance the mixing of the filler metal in LBW. In the study of Gatzen (2012), the filler metal was significantly homogenized in the weld pool under a low-frequency (below 25 Hz) coaxial alternating magnetic field. In the authors' previous research, a transverse oscillating magnetic field in the kilohertz range was imposed at the top side of the workpiece during LBW of austenitic steel. The additional Ni from the filler wire was successfully transferred to the root of the weld pool under the downward Lorentz force (Meng *et al.* 2019a).

The MHD technique has also shown the effectiveness of eliminating or suppressing interior defects. A transverse oscillating magnetic field with 4 kHz frequency was applied to a partial penetration LBW of Al in the work of Fritzsche *et al* (2018). A porosity reduction of above 70%, as well as evident surface stabilization, was achieved. It was suggested that the keyhole was stabilized by the magnetic field, which mainly contributed to the porosity mitigation (Huang *et al.*, 2020). Note that the keyhole geometry was observed by the metal/glass configuration in the works of Huang *et al.*

(2020) and Üstündağ et al. (2021). The unmelted and adiabatic glass worked as a symmetrical boundary in the setup, which had good physical accordance with the heat transfer and fluid flow in a realistic LBW process. The non-conducting glass, however, changed the electrical condition, thereby the deviation should be carefully evaluated.

As the improvement of the computational capacity, more multi-physical modeling works have been performed to describe the influence of the magnetic field on the LBW process and moreover to correlate the influenced weld pool behavior with the resulting defect mitigation. To simplify the complex physics involved, most of the available researches were conducted with a fixed keyhole geometry. A three-dimensional numerical model was developed by Bachmann *et al.* (2013) to study the effect of electromagnetic support in the LBW under a steady or oscillating magnetic field. The influence of the orientations of the steady magnetic field on the weld pool in the LBW of Al was investigated numerically by Chen *et al.* (2018a). By considering the Seebeck effect, Chen *et al.* (2018b) calculated the induced thermoelectric currents and thermoelectric-magnetic effects. The enhancement of the metal mixing by a coaxial magnetic field during LBW with filler wire was calculated and analyzed using a numerical model developed by Gatzen *et al.* (2011). It was found that the frequency determined the distribution pattern of filler material, and the magnetic flux density showed more significance on determining the homogeneity.

Clearly, the underlying keyhole dynamics and all the keyhole-relevant phenomena, e.g., transient laser absorption, porosity formation, etc., cannot be reproduced by the model with a fixed keyhole shape. Recently, the MHD effect on the LBW was studied with the multi-physical models considering the dynamic keyhole self-consistently with the free surface tracing algorithm, which provided a deeper insight into the physics of the process (Chen et al., 2019, Cao et al., 2020). Thereby, the mechanism of the MHD effect on the defect mitigation can be analyzed more comprehensively. Zhang *et al.* (2021) studied the influence of an oscillating magnetic field on the suppression of the weld root hump in the full penetration LBW of Al by a CFD model coupled with the volume-of-fluid method. The electromagnetic support not only showed an effective impact on the thermal fluid flow in the weld pool but also could directly change the collapse position of the keyhole. A multi-physical model was developed in the authors' works to study the EMS effect on the material mixing in wire feed LBW (Meng et al. 2019b). The weld pool behavior, especially for the element transport, with and without magnetic field were compared to explain the enhancement of the element homogeneity.

Current studies principally focus on the thermo-fluid flow of the bulk molten metal in the weld pool under the impact of the Lorentz force. The influence of the MHD effects on the keyhole dynamics was only reported in a few research works (Huang et al., 2020; Üstündağ et al., 2021), and

an in-depth discussion has not yet been possible. The objective of the paper hereby is to understand better the keyhole dynamics, such as laser energy absorption, keyhole geometry, keyhole fluctuation, etc., under an external oscillating magnetic field, using experimental and multi-physical modeling methods. The micro-X-ray computed tomography (μ -CT) measurement confirmed a significant reduction of porosity under the MHD effect. For the first time, an attempt was made to quantitatively rationalize the mitigation of keyhole-induced porosity associated with the keyhole dynamics and the thermo-fluid flow in the weld pool under the influence of a magnetic field. The findings provide valuable insights into understanding the correlation with electromagnetic parameters, keyhole dynamics, and suppression of keyhole-relevant defects.

2. Experimental and numerical methodologies

2.1 Experimental setup of LBW with a magnetic field

304 stainless steel with austenitic microstructure was used as the base metal with a dimension of 200 mm \times 60 mm \times 10 mm. The nominal chemical compositions of material used are given in Table 1. A butt welding was conducted with an IPG fiber laser system of 20 kW maximum output. The laser beam with 1070 nm wavelength and 0.52 mm beam diameter irradiated vertically the top surface of the workpiece. The laser power was set to 6.5 kW and the welding speed was 1.3 m/min. Pure Argon with 20 l/min flowrate was provided behind the laser spot to protect the weld seam from oxidation. Mechanical cleaning on the workpiece surface was performed before welding to minimize the formation of metallurgical porosity.

Table 1 Nominal composition of 304 steel (wt.%)

Alloy	Ni	Cr	Mo	Nb	C	Si	S	Fe
304 steel	8.0-10.0	17.5-19.0	-	-	<0.07	<0.75	<0.015	bal.

The oscillating magnetic field was generated with an in-house developed alternating current (AC) electromagnet. The electromagnet which had a 20 mm gap between the magnet poles was installed 2 mm above the base metal, whereby a transverse magnetic field could be introduced into the weld pool, as shown in Fig.1(a). Based on the optimization in our previous study (Meng et al., 2019a), the magnetic flux density, the frequency, and the orientation were selected as 250 mT, 3575 Hz, and 15 deg with respect to the transverse direction, respectively.

2.2 High-speed cameral imaging

To obtain the real-time sub-face weld pool geometry, a configuration of steel and quartz glass was utilized, as shown in Fig. 1(b), in which the high heat-resistant but low heat-conducting quartz glass operated as a symmetric plane for the heat and mass transfer. A Fastcam 1024 high-speed camera operating at 3000 frames/s was used to capture the internal weld pool shape through the observation window provided by the transparent quartz glass. The camera was equipped with a bandpass filter at 808 ± 1.5 nm to suppress the interference of intensive light from incident laser radiation and vapor/plasma on the imaging signal. The optical axis of the lens was vertical to the metal/glass interface.

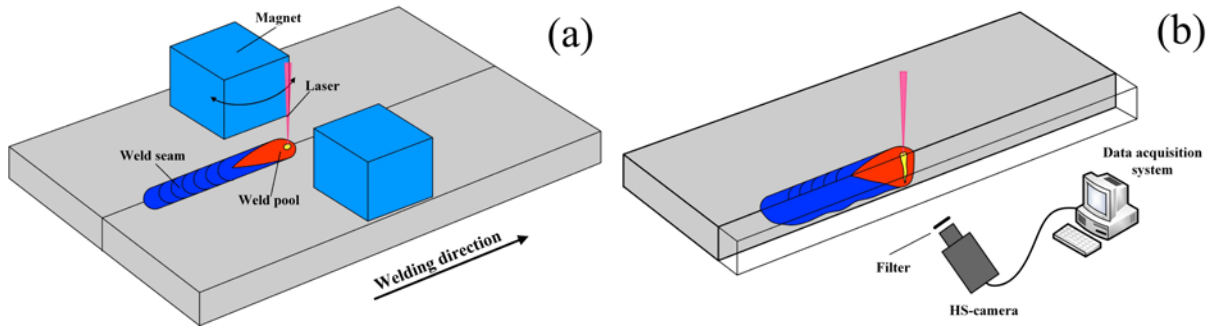


Fig. 1 (a) schematic of LBW experiment system, (b) schematic of metal/glass observation system

2.3 Characterization

The weld specimen was mechanically cut, ground, and polished on the cross-section, and subsequently etched with a V2A etchant (100 ml H₂O, 100 ml HNO₃, and 10 ml HCl). An optical microscope was used to observe the fusion line shape on the cross-section.

The μ -CT measurements were performed to investigate the three-dimensional distribution of the pores and their morphology. The samples with a dimension of 60 mm \times 6 mm \times 10 mm were prepared from the weld specimen by mechanical cutting, and a region of 30 mm \times 6 mm \times 10 mm in dimension was selected as the scanning volume. A voltage of 215 kV and a current of 100 μ A were used during the measurement, which achieved a resolution of 10 μ m. A total of 3000 radiographic projections were taken during a full rotation for each sample to reconstruct the 3D image.

2.4 Multi-physical modeling

A 3D CFD model coupled with MHD and VOF modules is developed in this paper to calculate the heat transfer, fluid flow, free surface deformation, as well as the electromagnetic behavior during LBW with a magnetic field. The model assumes that the Reynolds number of the liquid metal in the weld pool is sufficiently low such that a laminar solver is appropriate according to the work of

Panwisawas et al. (2017). The base metal maintains completely non-ferromagnetic (Bachmann et al., 2014), and the vapor plume is weakly ionized so that can be assumed as non-conductive (Kawahito et al., 2008). A brief summary of the theoretical framework is given in the following.

The free surface tracing is realized by the VOF algorithm from Hirt and Nichols (1981), which is governed by the following equation:

$$\frac{\partial \phi}{\partial t} + \nabla \cdot (\vec{v} \phi) = 0 \quad (2)$$

where t is the time and ϕ is the volume fraction of different phases, namely Ar gaseous phase and steel phase in this study. The free surface is located and reconstructed based on the spatial distribution of the volume fraction. It should be noted that although a gas phase is present in the model, the metal evaporation is not directly simulated.

The Navier-Stokes equations together with the mass conservation equation describe the liquid flow in the model. These can be written as:

$$\nabla \cdot \vec{v} = 0 \quad (3)$$

$$\rho \left(\frac{\partial \vec{v}}{\partial t} + \vec{v} \cdot \nabla \vec{v} \right) = -\nabla p + \mu \nabla^2 \vec{v} - \mu K \vec{v} + \vec{S}_m + F_{\text{surface}} \quad (4)$$

where \vec{v} is the liquid velocity vector, ρ is the density, p is the pressure, μ is the dynamic viscosity, K is the Carman–Kozeny equation coefficient for the enthalpy-porosity solidification model, \vec{S}_m is a volumetric force term including gravity, buoyance, and the Lorentz force density induced by the MHD effect. The F_{surface} term represents the converted volumetric forces from the original surface forces, and acts only on the metal/gas interface. A number of physical mechanisms contribute to the F_{surface} term in the present study, e.g., recoil vapor pressure, surface tension, and Marangoni stress. The continuum surface force (CSF) method from the work of Brackbill et al. (1992) is applied for the conversion, which can be written as:

$$F_{\text{surface}} = \left[\frac{AB}{\sqrt{T}} \exp\left(-\frac{m\Delta L_v}{R_g T}\right) + \gamma \kappa + \frac{\partial \gamma}{\partial T} \frac{\partial T}{\partial \vec{s}} \right] \tilde{\phi} \quad (5)$$

Here the first, second and third terms in the square brackets represent the recoil pressure, capillary pressure from the surface tension and the Marangoni stress, in which A and B are material-dependent evaporation coefficients, which are taken as $0.55 \text{ K}^{1/2}$ and $3.9 \times 10^{12} \text{ kg/m} \cdot \text{s}^2$ for pure iron, respectively; m is the molar mass, ΔL_v is the evaporation latent heat, R_g is the ideal gas constant, γ is the surface tension coefficient, κ is the curvature and \vec{s} is the tangential vector of the keyhole surface. $\tilde{\phi}$ is the CSF conversion operator which can be expressed as:

$$\tilde{\phi} = \frac{2\nabla F [\phi \rho_{\text{steel}} + (1-\phi) \rho_{\text{Ar}}]}{(\rho_{\text{steel}} + \rho_{\text{Ar}})} \quad (6)$$

The heat transfer behavior is governed by the energy conservation equation, given as follows:

$$\rho \left[\frac{\partial h}{\partial t} + (\vec{v} \cdot \nabla) h \right] = \nabla \cdot (k \nabla T) + Q_{\text{surface}} \quad (7)$$

Here T is the temperature, k is the thermal conductivity, h is the enthalpy. Similar to Eq. (3), Q_{surface} is the converted volumetric heat from the surface heat flux, which is given as:

$$Q_{\text{surface}} = \left[q_L - h_c (T - T_0) - \sigma \varepsilon_r (T^4 - T_0^4) - \rho v_{\text{evp}} \Delta L_v \right] \tilde{\phi} \quad (8)$$

where q_L is the laser heat flux, h_c is the convective heat loss coefficient, σ is the Stefan-Boltzmann constant, ε_r is the emissivity, and v_{evp} is the free surface recession speed due to evaporation. The spatial distribution of laser energy is calculated by a ray-tracing algorithm with a virtual refinement technique to consider the dominant features of the laser beam, i.e., multiple reflections and Fresnel absorption (Cho et al., 2012).

An improvement on the existing ray-tracing method is proposed in this paper for a higher algorithm's accuracy and robustness. Typically, a geometrical criterion is employed in the ray-tracing algorithm with a VOF-based free surface to identify the target reflection cell, rather than calculating the exact reflection point. The criterion can be written as $d \leq \sqrt{3}\Delta/2$, where Δ is the cell size (Cho and Na, 2006). The Ray II in Fig. 2(a) shows the situation where the reflection cell is found correctly. However, the identification may be physically incorrect when the incident angle is close to 90 degrees, as shown by the red Ray I. Ray I is captured by the neighbor cell before it reaches the right reflection cell. The error which is caused by a combination of vertical laser beam and steep keyhole wall is highlighted by the red dash-line box in Fig. 2(b), where a certain number of rays are trapped at the keyhole wall.

Therefore, an additional criterion is applied here to exclude the reflection cell which does not obey the optical laws. This can be realized by judging the angle between the incident ray and the outward normal vector. For the physically incorrect cell, e.g., the neighbour cell marked by the red dash circle in Fig. 2(a), the angle between the incident ray and the outward normal vector (angle α) is less than 90 deg. In contrast, the angle in the correctly identified cell is always larger than 90 deg. After implementing the additional criterion, the trapping of the rays is eliminated, providing a more reasonable energy distribution in the keyhole, see Fig. 2 (c)

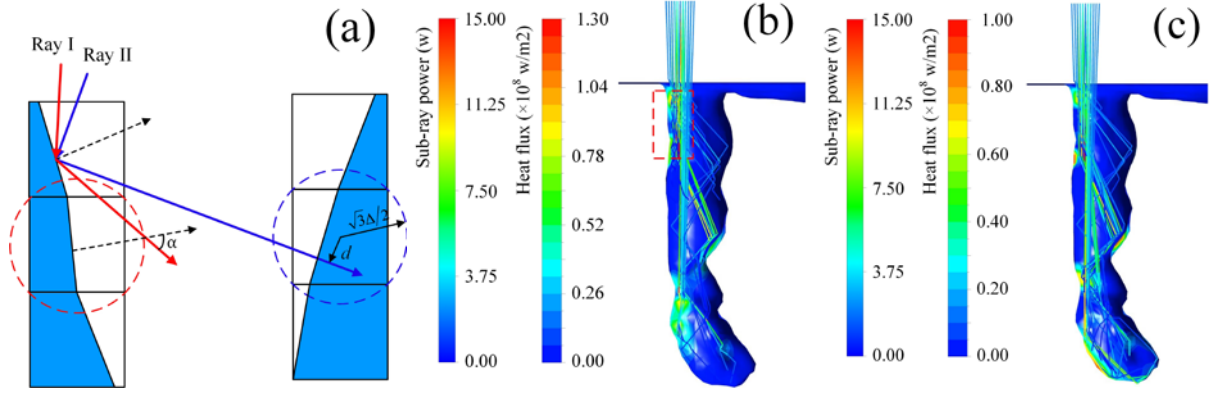


Fig. 2 (a) schematic of the incorrect identification of the reflection cell, (b) laser energy distribution without angle criterion, (c) laser energy distribution with angle criterion

The MHD effect induced by both temporal variation of the magnetic field and the liquid movement is described by the following equations:

$$\frac{\partial \vec{b}}{\partial t} + (\vec{v} \cdot \nabla) \vec{b} = \frac{1}{\mu_m \sigma_e} \nabla^2 \vec{b} + \left((\vec{B}_0 + \vec{b}) \cdot \nabla \right) \vec{v} - (\vec{v} \cdot \nabla) \vec{B}_0 \quad (9)$$

$$\vec{F}_L = \vec{j} \times \vec{B} = \frac{1}{\mu_m} \nabla \times (\vec{B}_0 + \vec{b}) \times (\vec{B}_0 + \vec{b}) \quad (10)$$

where μ_m is the magnetic permeability, σ_e is the electrical conductivity, \vec{b} is the induced magnetic field from the liquid flow, and the temporal variation of the external magnetic field \vec{B}_0 , \vec{F}_L is the Lorentz force density.

By solving Eqs. (2)~(10), the evolution of the keyhole dynamic and weld pool behavior under the MHD effect can be analyzed and rationalised. The boundary condition, numerical algorithms and model parameters are adopted from the authors' previous works, see the work of Meng et al. (2021).

4. Results and discussion

4.1 Keyhole dynamics under MHD effect

Fig.3 shows the comparison of the cross-section with and without the influence of the magnetic field. A decrease of penetration depth from 7.6 mm to 6.7 mm is produced by the MHD effect, whereas a widening of the weld seam from 4.3 mm to 5.3 mm can be observed. It implies that either the direct laser absorption or the heat transfer in the weld pool is influenced by the magnetic field. The in-situ weld pool profiles obtained by the metal-glass technique are given in Fig. 4. A unique profile can be seen in Fig. 4(a) for the normal LBW where the weld pool is characterized by a swelling at the bottom region and a significant narrowing at the middle region. This feature was

recently confirmed in the experimental observation of Wang et al. (2018). The swelling, also known as bulging, and the narrowing were found as the inducing factors for the formation of hot cracking and inhomogeneous element distribution (Artinov et al., 2019). Under the MHD effect, the top region of the weld pool is enlarged, and correspondingly, the bottom circulation is suppressed.

It must be noted that the longitudinal section shown in Fig. 4(b) is not the theoretical symmetric plane, although the laser beam center is located exactly on the steel/glass interface. This is because the electrically non-conducting quartz glass does not serve as a symmetric boundary for the electromagnetic field. The skin effect occurs in the electrically conducting media under an oscillating magnetic field, which makes the magnetic field apt to concentrate at the surface region. The dissimilarity of the magnetic flux density between the steel and glass sides changes the original symmetry of the weld pool. The impact can hardly be evaluated, making the quantitative comparison between Fig. 4(a) and (b) challenging. Nevertheless, it can still be confirmed qualitatively that the MHD effect brings a noticeable influence on the keyhole dynamics and the weld pool behavior.

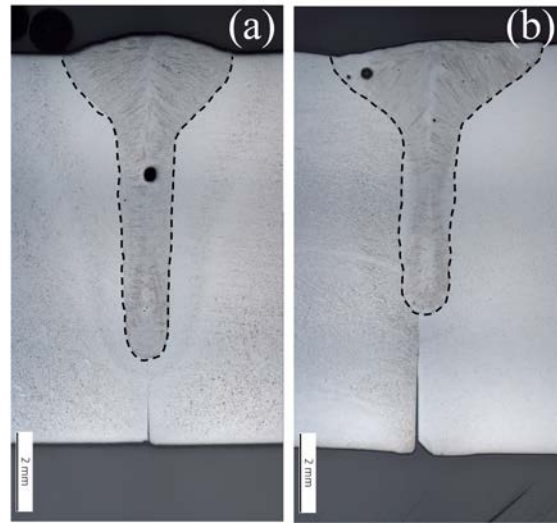


Fig. 3 Influence of magnetic field on the weld cross-section: (a) normal LBW, (b) LBW with a magnetic field

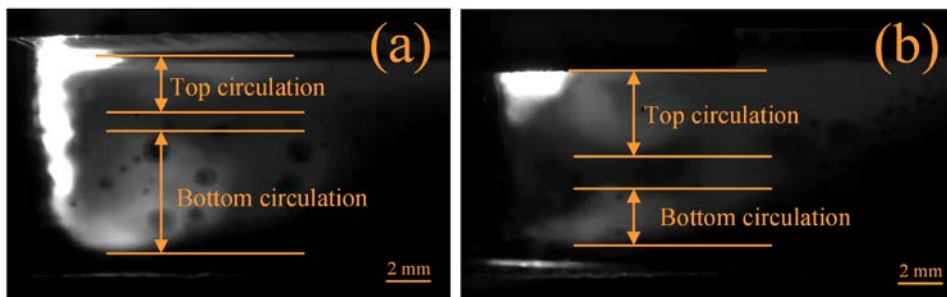


Fig. 4 Influence of magnetic field on the weld pool profile obtained by meta/glass observation: (a) normal LBW, (b) LBW with a magnetic field

The multi-physical model developed in this paper provides a predictive capability to allow for a better understanding of the keyhole dynamics and the sub-surface weld pool behavior under the MHD effect. Fig. 5 shows the comparison between the calculated and the experimental fusion lines. Overall, the numerical predictions are in good agreement with the experimental results for the reference case and MHD case. More specifically, the model successfully reproduces the decrease of the penetration depth and the widening of the weld seam caused by the magnetic field. However, the MHD effect is underestimated to a certain extent in the model as the deviation for the MHD case is relatively larger.

The calculated longitudinal section of the weld pool for normal LBW is compared with the experimental observation in Fig. 6. Not only the calculated weld pool length is close to the realistic value, but also the narrowing at the middle region and the bulging at the bottom region are predicted by the numerical model, which further proves the model's physical rationality.

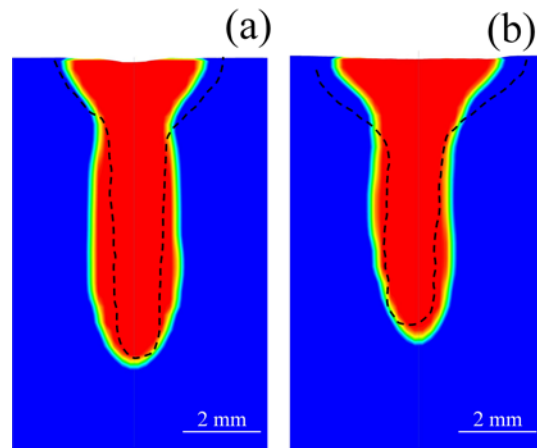


Fig. 5 Comparison of calculated and experimental (black dashed line from Fig.3) fusion lines: (a) normal LBW, (b) LBW with a magnetic field

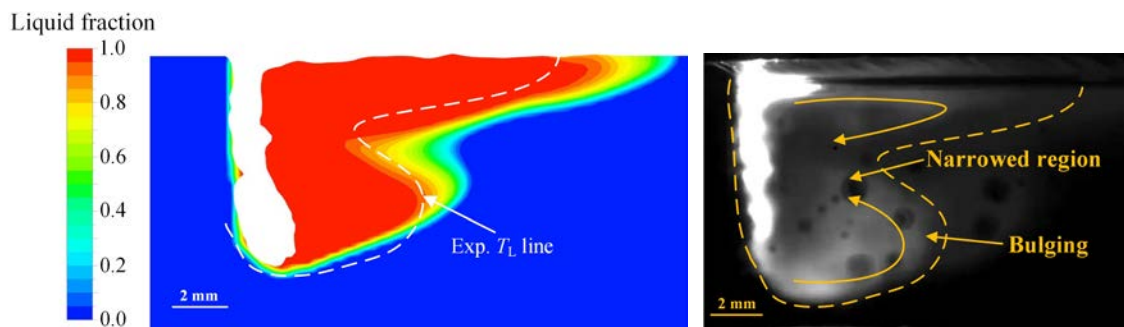


Fig. 6 Comparison of weld pool profiles for normal LBW

A periodic Lorentz force with a frequency of 7150 Hz which is two times the magnetic field frequency is produced. The time-variant induced Lorentz force density in the vertical Z direction at point P is plotted in Fig. 7. The curve shows a regular sinusoidal shape, and the downward force ($3 \sim 4 \times 10^5 \text{ N/m}^3$) is stronger than the upward force ($2 \sim 2.5 \times 10^5 \text{ N/m}^3$). The whole weld pool experiences periodic expansive forces and compressive forces with a maximum magnitude of $3.7 \times 10^6 \text{ N/m}^3$ and $5.7 \times 10^6 \text{ N/m}^3$, respectively. The Lorentz force reduces exponentially along the thickness direction due to the skin effect. From a time-averaged term, the applied oscillating magnetic field provides a downward Lorentz force in the weld pool, which is consistent with current research results, see the work of Bachmann et al. (2014).

Periodic expansive and compressive forces are generated on the keyhole wall as well. Yet, the distribution pattern is more irregular and complex because of two factors: firstly, the keyhole wall is the boundary between electrically conducting and non-conducting materials, namely steel and Ar gas; secondly, the high temperature gradient on the keyhole wall makes the electrical conductivity extremely uneven. A downward Lorentz force with a maximum force density of $9.5 \times 10^5 \text{ N/m}^3$ is formed at the keyhole opening, which may directly influence the laser energy absorption. The transient Lorentz force density distribution in the weld pool and on the keyhole wall can be found in the supplementary materials provided, see videos 1 and 2. The corresponding real physical time in the videos is about 0.3 ms.

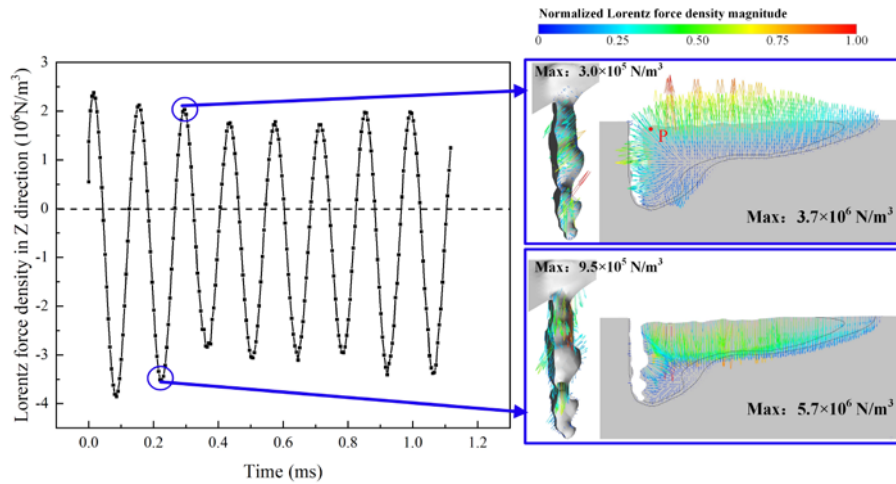


Fig. 7 Calculated Lorentz force density distribution

The time-variant averaged keyhole diameter which is defined as $d_{aver} = \sqrt{4V_{keyhole} / (\pi H_{keyhole})}$, where $V_{keyhole}$ is the internal volume of the keyhole and $H_{keyhole}$ is the keyhole depth, is given in Fig. 8. The compressive Lorentz force leads to a decrease of the keyhole diameter from 0.96 mm to 0.87 mm. It is indicated that a Lorentz force density with a magnitude of $5 \sim 10 \times 10^5 \text{ N/m}^3$ is sufficient to

change the keyhole profile, while it is usually believed that the keyhole profile is dominated by the recoil pressure (Kawahito et al., 2008).

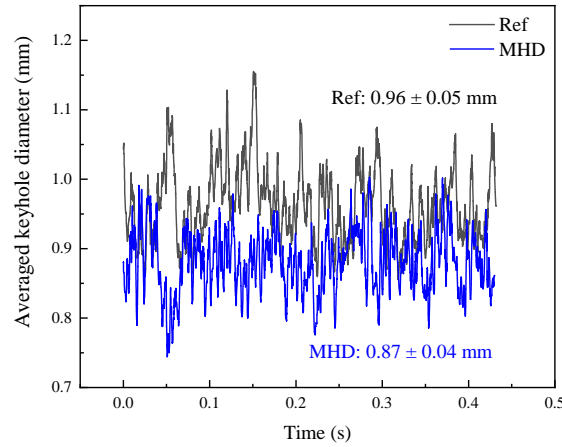


Fig. 8 Time-variant averaged keyhole diameter.

Fig. 9 provides a deeper look at the transient energy absorption and the alteration produced by the MHD effect. The location of maximum downward flow occurring on the keyhole wall versus time is plotted. This is also the location that is under the direct laser beam irradiation, thus receiving the highest energy. The detailed laser energy distribution and the velocity field at certain time points are provided below, corresponding to the red points in the time sequence. As seen in Fig. 9(a), small protrusions are formed on the fluctuating front wall, and the top surface of the protrusion will be exposed under the direct irradiation of the laser beam. The protrusions will then be driven downward to the keyhole bottom by the induced recoil pressure, as marked by the red circles. In other words, the laser beam can reach the keyhole bottom at this time. Lately, this alternate melting between keyhole wall and keyhole bottom was also found in the experimental work of Wang et al. (2021).

Rapid downward movement of the protrusion can also be observed during LBW with a magnetic field, but this procedure may be interrupted as seen in Fig. 9 (b). Under the disturbance from the Lorentz force, a new protrusion may form before the old protrusion reaches the keyhole bottom, blocking the downward propagation of the laser beam. It can be expected that the laser energy distribution could be adjusted by changing the keyhole front wall behavior with a suitable MHD effect.

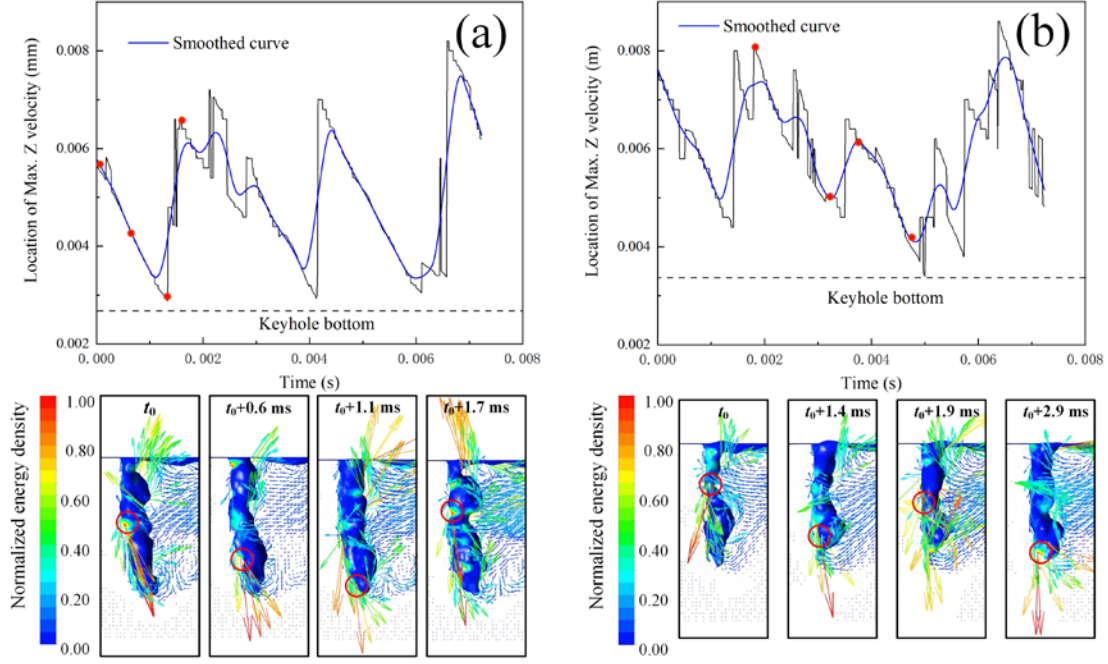


Fig. 9 Transient laser energy distribution and liquid flow on the keyhole wall: (a) normal LBW, (b) LBW with magnetic field

Since the laser energy is highly uneven on the keyhole wall and varies transiently (Tan et al., 2014), an arbitrarily selected distribution at a certain time point may show lower statistical accuracy. Thus, the time-averaged laser energy distribution within 200 ms is given in Fig. 10. Note, the keyhole profile (black line) shown in the figure is instantaneous and is provided only for an intuitive expression of the relative position. Part of the laser energy ($\sim 35\%$) is absorbed by the keyhole front wall, and several discontinuous high-energy spots form there. It is close to the experimentally measured value of $35\% \sim 43\%$ from Matti and Kaplan (2015). The rest of the energy is distributed relatively homogeneously in the keyhole volume due to the multiple reflections. After introducing the magnetic field, more laser energy is absorbed in the top region of the keyhole, as shown in Fig. 10(b), which is closely related to the formation of the protrusions and their movement. The downward Lorentz force acting on the keyhole opening (see Fig. 7) may induce more protrusions and subsequently influence the laser beam propagation.

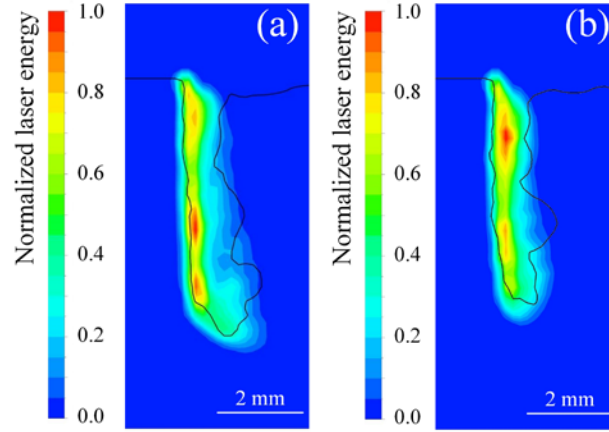


Fig. 10 Time-averaged laser energy distribution on the longitudinal section: (a) normal LBW, (b) LBW with magnetic field

Fig. 11 shows the time-averaged distribution of the total laser power distributed along the thickness direction, where the distance is normalized by the keyhole depth. By integrating the curves, it can be found that the MHD effect plays no role in the thermal efficiency, 71 % for the normal LBW vs. 70 % for the LBW with a magnetic field. More energy is absorbed in the middle column of the keyhole under the MHD effect. The distribution ratio of the laser energy for normal LBW is 21%, 50%, and 29% at the opening, middle and bottom regions, respectively. For comparison, the ratio is 19 %, 56 %, and 24 % in the LBW with a magnetic field.

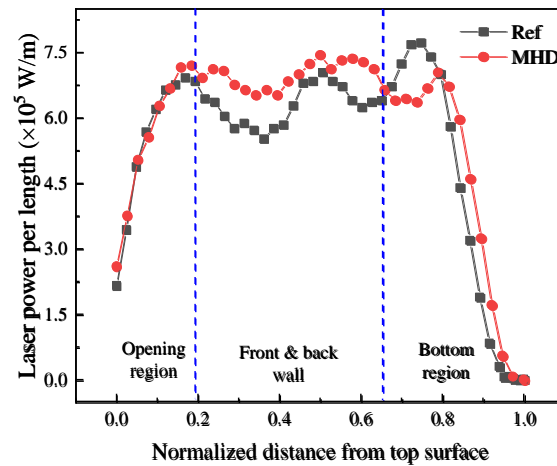


Fig. 11 Time-averaged distribution of total laser power along the thickness direction

4.2 Porosity mitigation by MHD effect

The 3D distribution of the porosity colored by the pore volume is shown in Fig. 12. A series of large pores with irregular shapes forms at the weld root, and spherical pores with relatively small

size ($0.05 \text{ mm}^3 \sim 0.10 \text{ mm}^3$) are distributed randomly within the weld seam. The extremely small pores with a volume less than 0.01 mm^3 are deduced to be metallurgical pores. A remarkable reduction of porosity ratio from 0.95 % to 0.24 % is produced by the MHD technique, which is close to the results presented by Fritzsche et al. (2018). All large pores are eliminated in the weld, and the maximum pore volume decreases from 0.26 mm^3 to 0.09 mm^3 .

It is also interesting that both the original pores in Fig. 12 (a) and the residual pores in Fig. 12(b) show a certain periodic distribution pattern. This fact implies that a periodic evolution of the keyhole and the weld pool occurs in both welding processes, in which two different mechanisms may be involved with and without magnetic field. It is worthy to be studied deeply in the future works.

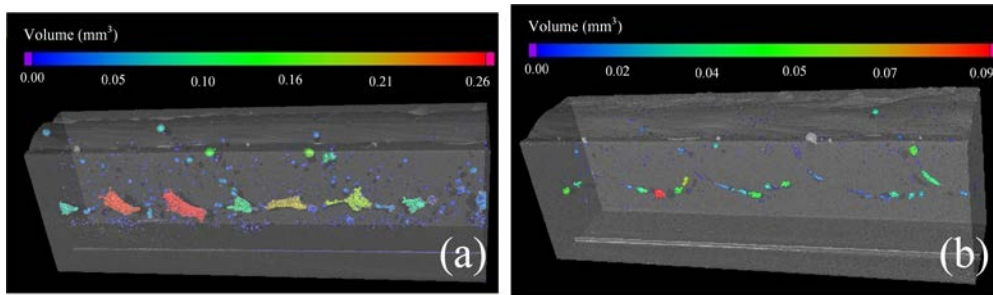


Fig. 12 3D porosity distribution measured by μ -CT scanning: (a) normal LBW, (b) LBW with a magnetic field

Different studies have tried to explain the suppression of porosity by the MHD effect from different aspects. Firstly, the magnetic field shows the direct influence on the keyhole dynamics, as described above and found by Huang et al. (2020) and Üstündağ et al. (2021), whereby the origin of the porosity, i.e., the bubble formation, may be inhibited. Secondly, an additional lifting force, named EM expulsive force, is exerted on the bubble to enhance the bubble escape from the liquid metal (Fritzsche et al., 2018). In addition, the solidification rate which is also a key factor to determine the porosity formation can also be altered by changing the weld pool profile (Meng et al., 2021). However, none of these explanations is comprehensive and quantitative. A first attempt will be given in this paper to analyze and decouple the multiple influences of the magnetic field on porosity mitigation using experimental and numerical data.

The study of Kawahito et al. (2017) suggested that the collapses occurring at the keyhole tip initiate the bubbles in the weld pool. In contrast, the collapse at the upper region is relatively easy to be reopened by the laser beam, which is irrelevant to the porosity formation. As shown in Fig. 13 (a), most of the collapses occur at the keyhole tip. If the condensation of the metal vapor in the bubble is ignored, implying that the bubble volume remains constant, the largest volume of the pores measured

by the μ -CT (0.26 mm^3) has an equivalent diameter of 0.8 mm. In the specific circumstance, 0 mm ~ 0.8 mm can be considered as a critical range, above which the collapse may not lead to a bubble in the weld pool, or the formed bubble can escape from the weld pool successfully.

Fig 13 (b) shows that the possibility distribution obeys a log-normal distribution with 87 % of the collapses happening at positions between 0 mm and 1.0 mm, in contrast to a standard normal distribution was reported by Pang et al. (2014). Fig. 13 (c) shows that more collapses occur in the upper region when a magnetic field was applied. The possibility distribution still obeys a log-normal form, but only 69 % of the collapses are located in the range between 0 mm and 1.0 mm, see Fig. 13(d). Therefore, the magnetic field brings stabilization to the keyhole from a viewpoint of porosity suppression by reducing the number of fatal bubbles.

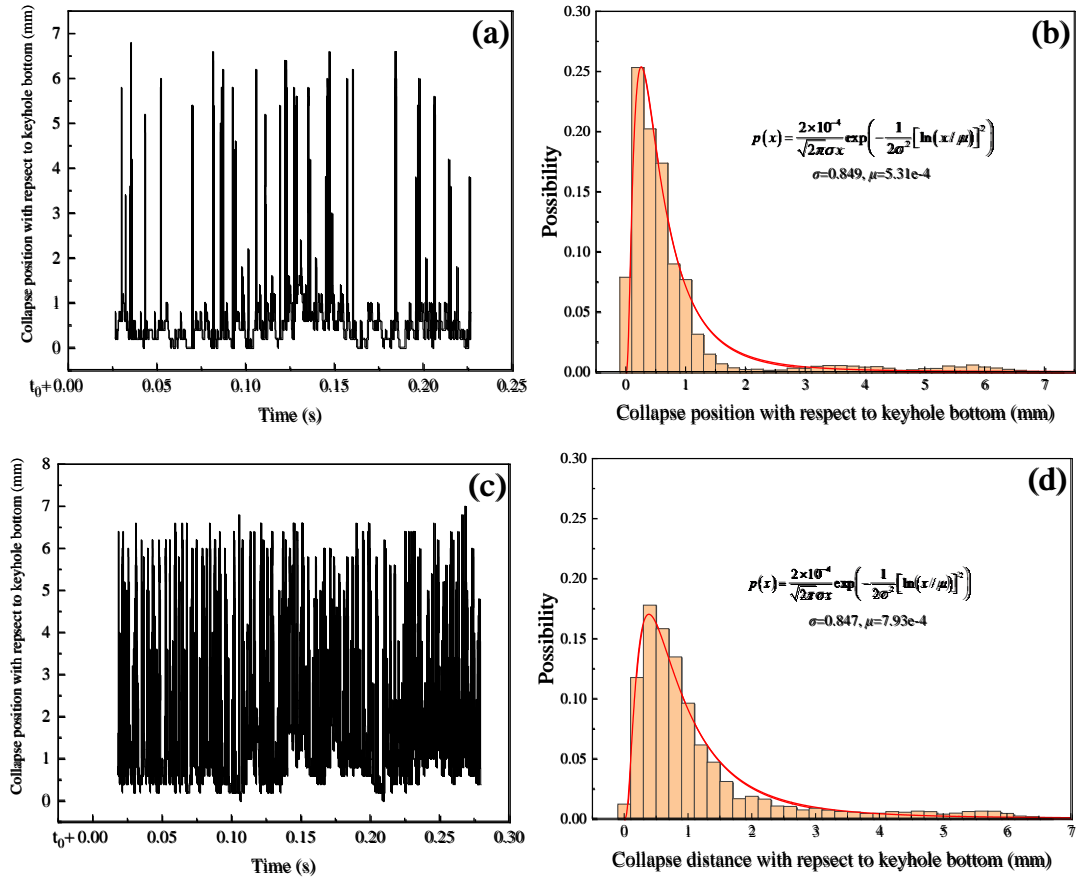


Fig. 13 Time-variant and statistical collapse position of keyhole: (a) and (b) for normal LBW, (c) and (d) for LBW with a magnetic field.

Next, the floating of the bubbles, which is determined by the bubble size, Lorentz force and the solidification rate, will be analyzed. Fig. 14 gives the projection of all pores on the longitudinal section and the corresponding weld pool profiles. The bulging and the narrowing phenomena are

almost eliminated by the MHD effect. It is worth noting that all the large pores with irregular shapes are trapped in the bulging region and the pores with relatively small diameter (0.3 mm ~ 0.4 mm) are captured by the liquid/solid front at the upper region, see Fig. 14 (a). As for the pores with a diameter of 0.2 mm ~ 0.4 mm in Fig. 14(b), they are mostly located at the bottom region where solidification time is the shortest.

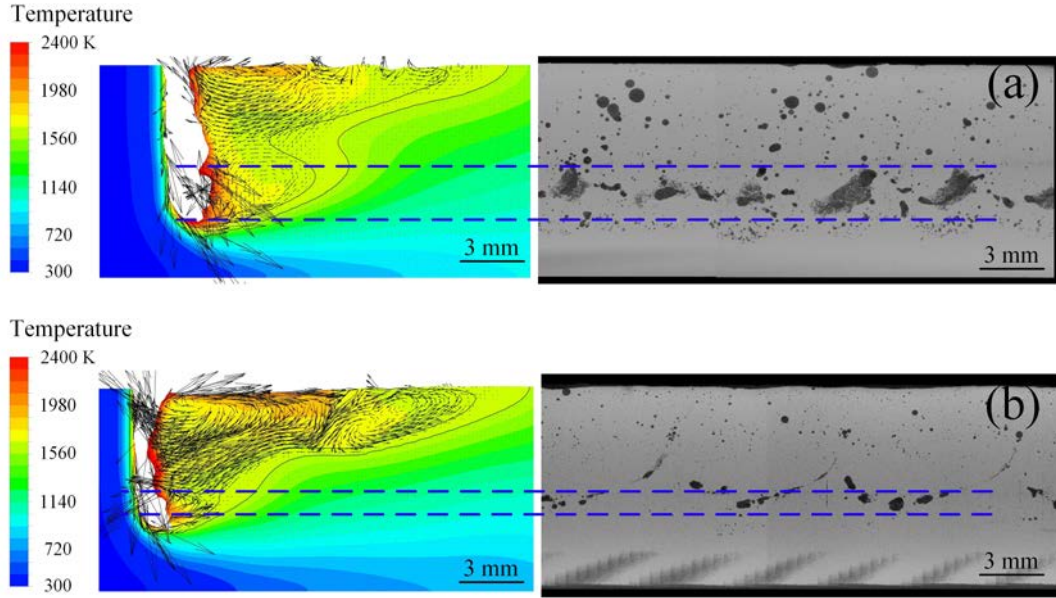


Fig. 14 Projection of porosity distribution on the longitudinal section and the corresponding weld pool profile: (a) normal LBW, (b) LBW with magnetic field

Let the liquid metal movement first be ignored, and the liquid regime belongs to the Stokes flow. A balance can be roughly built between buoyance, EM expulsive force and the viscous drag force from the liquid, which gives:

$$\frac{3}{4} \frac{\pi d_B^3}{6} F_L + \frac{4\pi}{3} \left(\frac{d_B}{2} \right)^3 \rho g = 3\pi \mu d_B v_{flo} \quad (11)$$

where d_B is the bubble diameter and v_{flo} is the floating velocity. Here the first term on the left-hand side is the EM expulsive force calculated by Leenov–Kolin’s theory (Takahashi and Taniguchi, 2003). Under a time-averaged downward Lorentz force, an upward expulsive force is produced. The second term is buoyance, which naturally helps the bubble to escape. The term on the right-hand is the total drag force on the bubble. The floating velocity can be estimated as:

$$v_{flo} = \frac{d_B^2}{\mu} \left(\frac{F_L}{24} + \frac{\rho g}{18} \right) \quad (12)$$

It shows that floating velocity is determined by both bubble size and the Lorentz force. The relative significance of the Lorentz force density and the buoyance are explicitly expressed.

A diagram of floating velocity under different bubble sizes and Lorentz forces density is plotted in Fig. 15, and several representative points are highlighted. The floating velocity increases with larger bubble size and larger Lorentz force. The buoyance alone provides a 0.50 m/s upward velocity for the large bubbles with an equivalent diameter of 0.8 mm, and the additional Lorentz force density of $3 \times 10^4 \text{ N/m}^3$ produces an extra floating velocity of 0.15 m/s. Both floating velocities should provide a sufficiently small floating time which is much smaller than the solidification time to guarantee the bubble escape. The large pores that remained in the final weld shown in Fig. 14(a) suggest that the bubbles are geometrically trapped by the narrowing in the middle region.

A floating velocity of 0.13 m/s is produced for the medium-sized bubbles solely by buoyance. A floating time of about 60 ms is required for bubble escape, and the critical solidification time is about 70 ms in comparison. Therefore, the medium-sized pores distributed at the upper region of the weld can be explained. An increase of floating velocity to 0.20 m/s is produced by applying a Lorentz force density of $6 \times 10^4 \text{ N/m}^3$, which provides a sufficiently small escape time of the bubbles. For the small bubbles with a diameter of 0.2 mm trapped in the weld bottom as seen in Fig. 14 (b), the bubbles have a floating velocity of 0.04 m/s under a Lorentz force density of $3 \times 10^4 \text{ N/m}^3$. This velocity is far below the necessary value for the bubble escape. As estimated by Eq. (12), a Lorentz force density in the magnitude of $5 \times 10^5 \text{ N/m}^3$ is required to drive the bubbles moving upward with a velocity of 0.13 m/s. It demands a magnetic field in the Tesla range, for which the electromagnetic equipment may have unpractical volume or energy consumption.

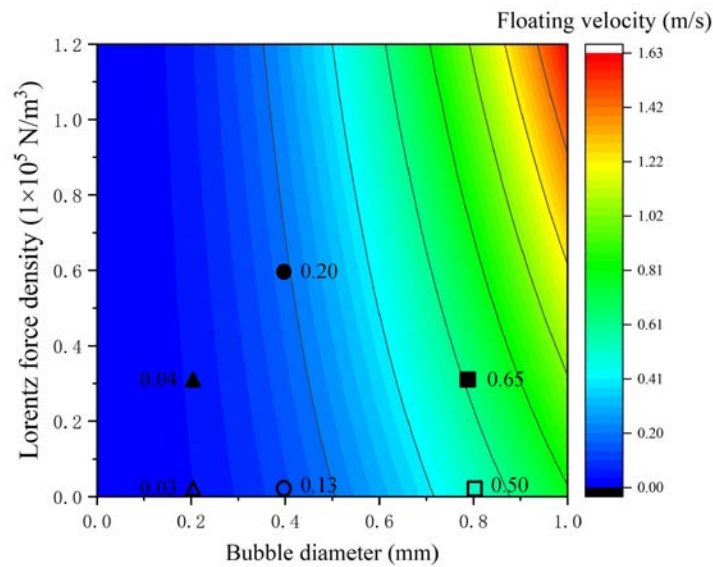


Fig. 15 Diagram of floating velocity considering bubble size and Lorentz force density

5. Conclusions

The influence of the magnetohydrodynamic (MHD) effect produced by an oscillating magnetic field on the keyhole dynamics has been studied in the present work, using experimental and multi-physical modeling approaches. An attempt is made to correlate the mitigation of the keyhole-induced porosity achieved by the MHD technique with the thermal dynamics in the weld pool. The specific conclusions are drawn below:

1. The MHD effect shows significant impacts on the penetration depth and weld pool profiles, which are also predicted successfully by the numerical model. The model can be interrogated further to analyze the keyhole dynamics and porosity mitigation.
2. The induced Lorentz force density in the range of 10^5 N/m^3 gives a direct influence on the keyhole diameter and the keyhole fluctuations. The movement of the protrusions on the front keyhole wall is altered under the disturbance of the Lorentz force, which is a key factor to determine the beam propagation. From a time-averaged viewpoint, more energy is absorbed in the upper region of the keyhole.
3. The micro-X-ray CT scanning indicates that the MHD technique achieves remarkable reduction on both pore size and porosity ratio.
4. The keyhole is stabilized by the magnetic field so that fewer collapses occur at the keyhole tip, forming fewer bubbles in the weld pool. The MHD effect provides the bubbles with a larger diameter ($> 0.6 \text{ mm}$) a fluent floating channel by widening the narrowing region of the weld pool. The medium-sized bubbles obtain a sufficient floating velocity under the EM expulsive force, while the small bubbles ($< 0.2 \text{ mm}$) remain trapped in the final weld.

Acknowledgment

This work is funded by the Deutsche Forschungsgemeinschaft (DFG, German Research Foundation)—Project No. 416014189 and No. 466939224.

References

- Artinov, A., Bakir, N., Bachmann, M., Gumenyuk, A., Na, S. J., Rethmeier, M., 2019. On the search for the origin of the bulge effect in high power laser beam welding, *J. Laser Appl.* 31(2) 022413.
- Bachmann, M., Avilov, V., Gumenyuk, A., Rethmeier, M., 2013. About the influence of a steady magnetic field on weld pool dynamics in partial penetration high power laser beam welding of thick aluminium parts, *Int. J. Heat Mass Transf.* 60 309-321.

- Bachmann, M., Avilov, V., Gumenyuk, A., Rethmeier, M., 2014. Experimental and numerical investigation of an electromagnetic weld pool support system for high power laser beam welding of austenitic stainless steel. *J. Mater. Process. Technol.* 214, 578-591.
- Brackbill, J. U., Kothe, D. B., Zemach, C., 1992. A continuum method for modeling surface tension. *J. Comput. Phys.* 100 (2) 335-354.
- Cao, L., Zhou, Q., Liu, H., Li, J., Wang, S., 2020. Mechanism investigation of the influence of the magnetic field on the molten pool behavior during laser welding of aluminum alloy. *Int. J. Heat Mass Transf.* 162, 120390.
- Chen, J., Wei, Y., Zhan, X., Pan, P., 2017. Weld profile, microstructure, and mechanical property of laser-welded butt joints of 5A06 Al alloy with static magnetic field support. *Int. J. Advanced Manu. Technol.* 92, 677-1686.
- Chen, J., Wei, Y., Zhan, X., Gao, Q., Zhang, D., Gao, X., 2018a. Influence of magnetic field orientation on molten pool dynamics during magnet-assisted laser butt welding of thick aluminum alloy plates. *Opt. Laser Technol.* 104, 148-158.
- Chen, J., Wei, Y., Zhan, X., Gu, C., Zhao, X., 2018b. Thermoelectric currents and thermoelectric-magnetic effects in full-penetration laser beam welding of aluminum alloy with magnetic field support. *Int. J. Heat Mass Transf.* 127, 332-344.
- Chen, X., Luo, M., Hu, R., Li, R., Liang, L., Pang, S., 2019. Thermo-electromagnetic effect on weld microstructure in magnetically assisted laser welding of austenite steel, *J. Manu. Process.* 41 111-118.
- Cho, J. H., Na, S. J., 2006. Implementation of real-time multiple reflection and Fresnel absorption of laser beam in keyhole, *J. Phys. D-Appl. Phys.* 39 (24) 5372.
- Cho, W. I., Na, S. J., Thomy, C., Vollertsen, F., 2012. Numerical simulation of molten pool dynamics in high power disk laser welding. *J. Mater. Process. Technol.*, 212(1), 262-275.
- Fritzsche, A., Hilgenberg, K., Teichmann, F., Pries, H., Dilger, K., Rethmeier, M., 2018. Improved degassing in laser beam welding of aluminum die casting by an electromagnetic field. *J. Mater. Process. Technol.* 253, 51-56.
- Gatzen, M., Tang, Z., Vollertsen, F., Mizutani, M., Katayama, S., 2011c. X-ray investigation of melt flow behavior under magnetic stirring regime in laser beam welding of aluminum. *J. Laser Appl.* 23, 032002.
- Gatzen, M., 2012. Influence of low-frequency magnetic fields during laser beam welding of aluminium with filler wire, *Phys. Procedia* 39, 59-66.
- Hirt, C. W., Nichols, B. D., 1981. Volume of fluid (VOF) method for the dynamics of free boundaries. *J. Comput. Phys.* 39 (1) 201-225.

- Huang, L., Liu, P., Zhu, S., Hua, X., Dong, S., 2020 Experimental research on formation mechanism of porosity in magnetic field assisted laser welding of steel. *J. Manu. Process.* 50 596-602.
- Kawahito, Y., Matsumoto, N., Mizutani, M., Katayama, S., 2008. Characterisation of plasma induced during high power fibre laser welding of stainless steel, *Sci. Technol. Weld. Join.* 13 (8), 744-748.
- Kawahito, Y., Uemura, Y., Doi, Y., Mizutani, M., Nishimoto, K., Kawakami, H., Katayama, S., 2017. Elucidation of the effect of welding speed on melt flows in high-brightness and high-power laser welding of stainless steel on basis of three-dimensional X-ray transmission in situ observation. *Weld. Int.* 31(3) 206-213.
- Kern, M., Berger, P., Huegel, H., 2000. Magneto-fluid dynamic control of seam quality in CO₂ laser beam welding. *Weld. J.* 79, 72-78.
- Matti, R. S., Kaplan, A. F., 2015. Post-modelling of images from a laser-induced wavy boiling front. *Appl. Surf. Sci.* 357 2277-2284.
- Meng, X., Bachmann, M., Artinov, A., Rethmeier, M., 2019a. Experimental and numerical assessment of weld pool behavior and final microstructure in wire feed laser beam welding with electromagnetic stirring. *J. Manu. Process.* 45, 408-418.
- Meng, X., Artinov, A., Bachmann, M., Rethmeier, M., 2019b. Numerical and experimental investigation of thermo-fluid flow and element transport in electromagnetic stirring enhanced wire feed laser beam welding. *Int. J. Heat Mass Transf.* 144, 118663.
- Meng, X., Bachmann, M., Artinov, A., Rethmeier, M., 2021. The influence of magnetic field orientation on metal mixing in electromagnetic stirring enhanced wire feed laser beam welding. *J. Mater. Process. Technol.* 294 117135.
- Pang, S., Chen, W., Wang, W., 2014. A quantitative model of keyhole instability induced porosity in laser welding of titanium alloy. *Metall. Mater. Trans. A* 45(6) 2808-2818.
- Panwisawas, C., Perumal, B., Ward, R. M., Turner, N., Turner, R. P., Brooks, J. W., Basoalto, H. C., 2017. Keyhole formation and thermal fluid flow-induced porosity during laser fusion welding in titanium alloys: Experimental and modelling, *Acta Mater.* 126 251-263.
- Takahashi, K., Taniguchi, S., 2003. Electromagnetic separation of nonmetallic inclusion from liquid metal by imposition of high frequency magnetic field. *ISIJ Int.* 43(6) 820-827.
- Tan, W., Shin, Y., 2014. Analysis of multi-phase interaction and its effects on keyhole dynamics with a multi-physics numerical model. *J. Phys. D-Appl. Phys* 47(34) 345501.
- Üstündağ, Ö., Bakir, N., Gumenyuk, A., Rethmeier, M., 2021. Influence of oscillating magnetic field on the keyhole stability in deep penetration laser beam welding. *Opt. Laser Technol.* 135 106715.

- Wang, H., Nakanishi, M., Kawahito, Y., 2018. Dynamic balance of heat and mass in high power density laser welding. *Opt. Express* 26, 6392-6399.
- Wang, Y., Jiang, P., Zhao, J., Geng, S., 2021. Effects of energy density attenuation on the stability of keyhole and molten pool during deep penetration laser welding process: A combined numerical and experimental study. *Int. J. Heat Mass Transf.* 176 121410.
- Xu, L., Tang, X., Zhang, R., Lu, F., Cui, H., 2020. Weld bead characteristics for full-penetration laser welding of aluminum alloy under electromagnetic field support. *J. Mater. Process. Technol.* 288, 116896.
- Zhang, R., Tang, X., Xu, L., Lu, F., Cui, H., 2021. Mechanism study of thermal fluid flow and weld root hump suppression in full penetration laser welding of Al alloy with alternating magnetic field support. *Int. J. Heat Mass Transf.* 166 120759.